J. Fluid Mech. (1999), *vol.* 385, *pp.* 229–254. Printed in the United Kingdom

Single drop impact onto liquid films: neck distortion, jetting, tiny bubble entrainment, and crown formation

By DANIEL A. WEISS[1,2]† AND ALEXANDER L. YARIN[1,3]

[1]Faculty of Mechanical Engineering, Technion – IIT, Haifa 32000, Israel

[2]Laboratoire PMMH, ESPCI, 10 Rue Vauquelin, 75231 Paris Cedex 05, France

[3]Department of Chemical Engineering and Rheology Research Center, University of Wisconsin, Madison WI 53706–1691, USA

(Received 20 June 1997 and in revised form 26 October 1998)

Single drop impact onto liquid films is simulated numerically. Surface tension and gravity are taken into account, whereas viscosity and compressibility are neglected. This permits recourse to a boundary-integral method, based on an integral equation for a scalar velocity potential. Calculations are performed for normal impacts resulting in axisymmetric flows.

For times that are small compared to the characteristic time of impact $2R/w_0$ (R being the drop radius, w_0 its initial velocity towards the liquid film), it is found that a disk-like jet forms at the neck between the drop and the pre-existing liquid film, if the impact Weber number is high enough. This jet can pinch off a torus-shaped liquid volume at its tip or reconnect with the pre-existing liquid film, thus entraining a torus-shaped bubble. In reality, both the torus-shaped bubble and liquid torus will decay according to Rayleigh's capillary instability, thus breaking the cylindrical symmetry. This mechanism of bubble entrainment differs from those described in literature.

For times that are comparable to or larger than the characteristic time of impact, capillary waves on the film, or the well-known crowns, are obtained again according to whether the impact Weber number is low or high enough.

1. Introduction

Drop impact onto solid and liquid surfaces is of widespread practical importance; it is related, for example, to ink-jet printing, soil erosion by rain, spray cooling, annealing, quenching and painting, shock atomization, combustion engines, meteorology, underwater noise of rain, etc. It has been investigated for more than a hundred years now. Worthington (1876, 1877, 1908) is generally considered as the first to investigate it systematically from a scientific point of view. Since then much work has been done; it was reviewed some years ago by Prosperetti & Oğuz (1993) and Rein (1993).

The various articles published so far concentrate on different impact conditions. These conditions can be high or low speed, deep or shallow liquids or hot or cold solids as targets, and so on.

It has been well known that according to these conditions, qualitatively different behaviours and phenomena can occur: the drops can spread over the solid surface

† Present address: Daimler-Chrysler AG, Research and Technology, PO Box 23 60, 89013 Ulm, Germany.

after impact (e.g. Chandra & Avedisian 1991; Fukai *et al.* 1993, 1995; Gao & Sonin 1994; Hatta, Fujimoto & Takuda 1995; Pasandideh-Fard *et al.* 1996; Schiaffino & Sonin 1997*a*, *b*; Waldvogel & Poulikakos 1997 – in several of these cases cooling and solidification of the spreading droplets are of primary importance); they can splash by creating a crown (e.g. Levin & Hobbs 1971; Yarin & Weiss 1995); a so-called Worthington jet or a vortex-ring can be formed (e.g. Shin & McMahon 1990; Dooley *et al.* 1997); droplet rebound and bouncing is possible (e.g. Foote 1975; Pasandideh-Fard *et al.* 1996; Hatta *et al.* 1997; Mao, Kuhn & Tran 1997), and so on. In several cases, one or more bubbles can be entrained by the drop impact. Pumphrey & Elmore (1990) compared four different mechanisms and scenarios of bubble entrainment. The so-called regular and irregular entrainment as well as large-bubble entrainment can occur only in the case of deep liquids. The Mesler entrainment resulting in a number of tiny bubbles (Esmailizadeh & Mesler 1986) was observed for the drop impact on deep liquids at low velocities only. For impact on shallow liquids, especially with relatively high velocities, we are not aware of any description of bubble entrainment in literature.

The crucial aspect of these phenomena is that a number of different hydrodynamic events takes place after the impact itself, i.e. during the spreading process of the liquid lamella (see Stow & Hadfield 1981; Yarin & Weiss 1995). Among these are surface waves on the lamella and formation of a crown.

In this work, we report on a numerical treatment of the drop impact onto films of finite thickness of the same liquid. The flow is considered to be a potential one, so the problem can be tackled by a boundary-integral method. For infinitely deep liquids as targets, a similar problem was treated by Oğuz & Prosperetti (1990). We compare our results with the predictions provided by means of a quasi-one-dimensional model developed in Yarin & Weiss (1995). Finally, we compare our results also with theoretical and experimental evidence available in literature.

In § 2 we formulate the problem and describe the initial conditions as well as the numerical technique and its implementation. The results are presented in § 3, where they are also discussed and compared with existing models and experiments. Section 4 contains concluding remarks.

2. Formulation of the problem and numerical implementation

Consider a spherical drop impinging perpendicularly onto a plane solid surface covered by a thin film. The drop consists of the same liquid as the film. The gravity field is supposed to act in the direction of the impact.

The phenomena to be considered here are highly transient. The timescales are not large enough for shear wave propagation across the liquid film on the wall, or across the free jet-like structures resulting from the impact. Detailed estimates will be given in § 3 in the discussion of the results. Thus we will prove *a posteriori* that viscous effects can be neglected (see also Oğuz & Prosperetti 1990; Yarin & Weiss 1995).

Furthermore, in the cases under consideration the fluid can be taken as incompressible. Compressibility effects are of importance only at the very first moments of impact, when the radius of the contact area of the drop $r_{contact}$ is of the order of $r_{contact} \lesssim r_c \approx w_0 R/c_0$ i.e. up to times after impact of the order of $t_c \approx Rw_0/(2c_0^2)$ (where R and w_0 denote the radius and velocity of the impacting drop, c_0 the velocity of sound in the liquid; see Bowden & Field 1964; Rein 1993; Yarin & Weiss 1995). For $R \approx 1$ mm, $w_0 \approx 1\ \mathrm{m\,s^{-1}}$ and $c_0 \sim 10^3\ \mathrm{m\,s^{-1}}$ we obtain $r_c \sim 1\,\mu\mathrm{m}$ and $t_c \sim 0.5$ ns, which already shows that compressibility effects are very short compared with the timescales typical of the impact, R/w_0, and even with $10^{-4} \times R/w_0$. In addition, the

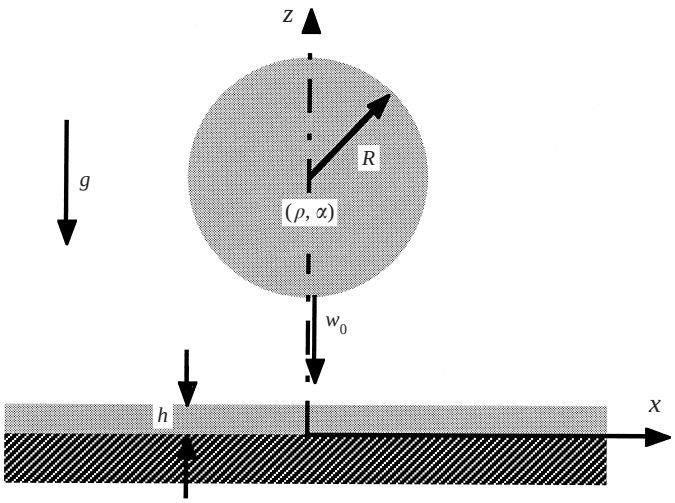

FIGURE 1. Drop impact onto a thin liquid film.

volume compressed by the shock wave at the time t_c after impact can be estimated by $\pi r_c^2 c_0 t_c \approx \pi/2\ R^3(w_0/c_0)^3 = \frac{3}{8}(w_0/c_0)^3 V_{drop}$, with V_{drop} being the volume of the impinging drop. This shows that, if $w_0/c_0 = O(10^{-3}) \ll 1$, compressibility affects a very small volume fraction of the impinging drop, i.e. that its effects can be neglected; indeed, compressibility effects have not been found experimentally at $w_0/c_0 = O(10^{-3})$.

The above estimates show that the impact Mach number w_0/c_0 is the crucial parameter for quantifying compressibility effects. Field, Dear & Ogren (1989) experimentally observed compressibility effects for a very high impact velocity $w_0 = 110\ \mathrm{m\,s^{-1}}$, which yields Mach numbers of the order of $O(10^{-1})$.

It is emphasized that even a small contact area of $r_c \sim 1\ \mu\mathrm{m}$ contains about $\pi r_c^2/\pi a^2 \approx 10^8$ molecules (a is a molecular size of the order of $10^{-10}\,\mathrm{m}$). The latter permits recourse to classical fluid mechanics even at this early stage (Lesser 1981; Lesser & Field 1983; Rein 1993). Also, the later incompressible stages of the impact process – with scales even larger than t_c, with which we are dealing in the present work – are obviously within the scope of classical fluid mechanics.

According to the estimates mentioned, the velocity field $\boldsymbol{u}$ is irrotational. It contains neither sources nor sinks and thus can be represented by a scalar potential Φ as per

$$\boldsymbol{u} = \operatorname{grad} \Phi(\boldsymbol{x}), \tag{2.1}$$

$$\Delta\Phi = 0, \tag{2.2}$$

for the interior of the fluid domain.

The normal fluid velocity vanishes at the impermeable wall, thus the boundary condition there is

$$\partial\Phi/\partial n = 0 \quad \text{at the solid wall}, \tag{2.3}$$

where $\boldsymbol{n}$ denotes the outer unit normal vector of the fluid domain.

The non-steady Bernoulli integral at the free surface of the fluid domain reads

$$\rho\partial\Phi/\partial t + \tfrac{1}{2}\rho\,(\operatorname{grad}\Phi)^2 + \rho g z + p = 0, \tag{2.4}$$

where ρ denotes the fluid density, g acceleration due to gravity (in the $-z$-direction, cf. figure 1), and p the pressure.

Assuming cylindrical symmetry of the whole process, we have only to consider the radial and axial coordinates, x and z, respectively, with x restricted to positive values. The solid wall is at $z = 0$.

From (2.1) and (2.4) we conclude that the boundary conditions at the free surface describing the evolution of its shape and the potential, read

$$\mathrm{D}x/\mathrm{D}t = \partial\Phi/\partial x, \tag{2.5a}$$

$$\mathrm{D}z/\mathrm{D}t = \partial\Phi/\partial z, \tag{2.5b}$$

$$\mathrm{D}\Phi/\mathrm{D}t = \tfrac{1}{2}\{(\partial\Phi/\partial x)^2 + (\partial\Phi/\partial z)^2\} - gz - p/\rho, \tag{2.5c}$$

where $\mathrm{D}/\mathrm{D}t = \partial/\partial t + \boldsymbol{u}\cdot\mathrm{grad}$ stands for the material time derivative. In particular, the condition (2.5c) permits updating the values of the potential at every fluid element at the free surface.

The derivatives $\partial\Phi/\partial x$ and $\partial\Phi/\partial z$ at the free surface are expressed in terms of the tangential and normal derivatives $\partial\Phi/\partial s$ and $\partial\Phi/\partial n$ by means of an orthogonal transformation:

$$\partial\Phi/\partial x = -\partial z/\partial s\ \partial\Phi/\partial n + \partial x/\partial s\ \partial\Phi/\partial s, \tag{2.6a}$$

$$\partial\Phi/\partial z = \partial x/\partial s\ \partial\Phi/\partial n + \partial z/\partial s\ \partial\Phi/\partial s, \tag{2.6b}$$

where s denotes the arclength measured from an arbitrary origin. For convenience, the origin of s is located on the axis of symmetry, namely at the apex of the impinging drop. Here, s is used as a parameter for the shape of the free surface.

Only the capillary component p_{cap} due to surface tension contributes to the pressure at the free surface in (2.4) and (2.5c):

$$p = p_{cap} = \alpha\kappa, \tag{2.7}$$

α being the surface tension and κ the mean curvature of the free surface. Expressing the curvature in terms of $x(s)$ and $z(s)$, we have

$$p = -\alpha\left(\frac{\partial^2 z}{\partial s^2}\frac{\partial x}{\partial s} - \frac{\partial^2 x}{\partial s^2}\frac{\partial z}{\partial s} + \frac{1}{x}\frac{\partial z}{\partial s}\right) \quad \text{if } x \neq 0. \tag{2.8}$$

The last term on the right-hand side has to be replaced by its limit at the symmetry axis:

$$p = -\alpha\left(\frac{\partial^2 z}{\partial s^2}\frac{\partial x}{\partial s} - \frac{\partial^2 x}{\partial s^2}\frac{\partial z}{\partial s} + \frac{\partial^2 z}{\partial s^2}\right) \quad \text{if } x = 0. \tag{2.9}$$

Here, we use the fact that $\partial x/\partial s = 1$ at $x = 0$, i.e. that the surface at the apex is smooth.

In our treatment, we render lengths dimensionless by the radius of the impinging drop R, velocities by $(gR)^{1/2}$, times by $(R/g)^{1/2}$, and the velocity potential by $(gR^3)^{1/2}$. The boundary conditions at the free surface become, according to (2.5)–(2.8),

$$\mathrm{D}x/\mathrm{D}t = -\partial z/\partial s\ \partial\Phi/\partial n + \partial x/\partial s\,\partial\Phi/\partial s, \tag{2.10a}$$

$$\mathrm{D}z/\mathrm{D}t = \partial x/\partial s\ \partial\Phi/\partial n + \partial z/\partial s\ \partial\Phi/\partial s, \tag{2.10b}$$

$$\mathrm{D}\Phi/\mathrm{D}t = \tfrac{1}{2}\{(\partial\Phi/\partial s)^2 + (\partial\Phi/\partial n)^2\} - z + S\left(\partial^2 z/\partial s^2\ \partial x/\partial s - \partial^2 x/\partial s^2\ \partial z/\partial s + 1/x\ \partial z/\partial s\right), \tag{2.10c}$$

the dimensionless group,

$$S = Bo^{-1} = \alpha/(\rho g R^2), \tag{2.11}$$

being the inverse Bond number.

Note that besides S, with the six dimensional parameters involved in the problem (w_0, R, g, h, α and ρ) we have two additional independent dimensionless groups, namely

$$H = h/R, \quad W = w_0(gR)^{-1/2}. \tag{2.12}$$

Another set of three independent dimensionless groups would be

$$Fr = w_0(gh)^{-1/2} = W\,H^{-1/2} \text{ (Froude number)}, \tag{2.13a}$$

$$H = h/R, \tag{2.13b}$$

$$We = 2R\rho w_0^2/\alpha = 2W^2S^{-1} \text{ (Weber number)}. \tag{2.13c}$$

With the choice (2.11) and (2.12), the evolution equations involve only one dimensionless group, namely S, whereas with the choice (2.13) all three groups Fr, H, and We would be involved, since $S = 2Fr\,H\,We^{-1}$.

We want to simulate numerically the evolution of the free surface itself (i.e. its x- and z-coordinates) as well as that of the potential Φ at the free surface according to the set of equations (2.10). Our method is based on an approach related to that introduced first by Longuet-Higgins & Cokelet (1976), Blake, Taib & Doherty (1986, 1987), and Oğuz & Prosperetti (1989).

If Φ is known on the surface of the fluid domain, $\partial\Phi/\partial s$ is obtained directly by tangential differentiation. To calculate the normal derivative $\partial\Phi/\partial n$ of Φ, which is also involved in the evolution equations (2.10), use is made of the fact that Φ is a harmonic function. Thus $\partial\Phi/\partial n$ may be found from the integral counterpart of the Laplace equation:

$$\Phi(\boldsymbol{x}) = \int \{G(\boldsymbol{x},\boldsymbol{x}')\;\partial\Phi/\partial n'\;(\boldsymbol{x}') - \Phi(\boldsymbol{x}')\;\partial G/\partial n'\;(\boldsymbol{x},\boldsymbol{x}')\}\mathrm{d}A', \tag{2.14}$$

with $\boldsymbol{x}$ on the boundary of the fluid domain. The integration covers the whole surface of this domain, including the wall. The vector $\boldsymbol{x}'$ stands for any point on it, including $\boldsymbol{x}' = \boldsymbol{x}$; $\mathrm{d}A'$ denotes the surface element at $\boldsymbol{x}'$, $\boldsymbol{n}'$ the outer unit normal vector at $\boldsymbol{x}'$ and G Green's function. The method of images is used to account for a plane rigid wall.

The integral equation (2.14) still contains an integral over the free surface; in the problem considered, integration in the azimuthal direction with respect to the symmetry axis can be carried out, leading to

$$\Phi(\boldsymbol{x}) = \int \{G_{eff}(\boldsymbol{x},\boldsymbol{x}')\;\partial\Phi/\partial n'(\boldsymbol{x}') - \Phi(\boldsymbol{x}')\;\partial G_{eff}/\partial n'(\boldsymbol{x},\boldsymbol{x}')\}\mathrm{d}s', \tag{2.15}$$

G_{eff} being the known effective Green function.

As we mentioned before, the fluid domain considered in (2.14) is bounded at the bottom by the solid wall and at the top by the free surface. Owing to the choice of Green's function in the method of images, there is no need to place nodes on the rigid surface. On the side, the fluid domain considered in (2.14) and (2.15) is bounded by a virtual cylindrical wall set across the liquid film at a distance l from the axis of impact. Treatment of the sidewall needs nodes – as well as, of course, the description of the free surface. The method with the virtual sidewall permits treatment of films of thickness comparable to, or even large with respect to, the drop radius – without a significant increase in the CPU-time needed.

Details of the numerical implementation of the boundary-integral equation (2.15) can be found in Weiss (1997). In previous works, treating free-surface flows with strong stretching and surface-tension effects, zigzag instability was encountered when

the boundary integral equation was employed (e.g. Longuet-Higgins & Cokelet 1976; Oğuz & Prosperetti 1990), and suppressed by numerical smoothing or by inclusion of artificial viscous terms. The numerical method of the present work permits calculations completely devoid of zigzag instability, even though no numerical smoothing or artificial viscous terms are used.

On the free surface, we work typically with 100 or 167 nodes, a reasonable compromise between accuracy and computation time consumption. We concluded this from comparison with the results obtained with 50 and 400 nodes. The virtual sidewall was typically at $l = 7$ in the calculations for the initial moments after impact, and at $l = 28$ in those for large times after impact. The number of nodes at the sidewall was taken between 2 and 12, depending on H.

At the moment of impact, the contact area between the drop and the film is a point, which inevitably creates serious problems in any numerical calculation. To avoid them, a segment of height $R(1-\beta)$ is cut from the oncoming drop. The remainder of the drop is assumed to hit the film directly, having thus an initial contact area of finite size. For the method to make sense, one has to require $0 < 1-\beta \ll 1$. In the calculations we used $\beta = 0.87, 0.90, 0.95$, 0.99 (standard), and 0.999. The effect of β is considered in the next section where the results of the calculations are discussed. Here, we mention only that the effect was minor.

The neck at the intersection between the sphere and the pre-existing liquid film is then smoothed out to avoid singularities in the capillary pressure. This is done by fitting a circle tangent to the sphere and the pre-existing liquid film. Its dimensionless radius r' is taken proportional to $(1-\beta)$, typically $\frac{2}{3}(1-\beta)$.

To determine the values of the potential, we bear in mind that the drop is to fall with a uniform velocity onto a quiescent film. Thus, at the moment of impact the potential is $\Phi = 0$ in the film, i.e. at $0 \leqslant z \leqslant h$, whereas it is $\Phi = -W(z-h)$ in the drop, i.e. at $z \geqslant h$. Such a distribution of the potential has a discontinuity in $\partial\Phi/\partial z$ and thus does not satisfy the Laplace equation. As was mentioned above, smoothing of the discontinuity and development of a finite contact area is related to compressible flow at the drop bottom. The velocity distribution generated by this flow still cannot be described by a harmonic function. Thus, at the moment when incompressible flow sets in (which we refer to as $t = 0$) the potential distribution over the free surface does not satisfy the Laplace equation. Only its asymptotic branches in the still unperturbed main parts of the drop and film are harmonic. Any non-harmonic function smoothly connecting these asymptotics may be used to generate the initial condition for Φ at the free surface, provided the compressible stage is not considered in detail. It is emphasized, however, that, at any moment $t > 0$, this initial distribution generates a harmonic potential in the whole fluid domain, since the Laplace equation is solved, which is precisely the way the potential flow develops in reality.

In the numerical implementation it should be checked whether a specific smoothing function has any effect on the results. Accordingly, we tested three such functions (exhibiting, of course, the same asymptotic behaviour in the unperturbed parts of the drop and film). In the first of these, at the neck between the drop and the film we chose a quadratic behaviour with respect to z, and on the sphere a linear behaviour (with a view to a uniform impact velocity), shifted by some amount to ensure continuity of the potential at the connection with the neck. This results in

$$\Phi(x, z; t=0) = \begin{cases} 0 & \text{for } z \leqslant h, \\ -W(z-h)^2/[2(z_0-h)] & \text{for } h \leqslant z \leqslant z_0, \\ -W(z-h/2-z_0/2) & \text{for } z \geqslant z_0, \end{cases} \tag{2.16}$$

where z_0 is the z-coordinate of the connection between the neck and the sphere. For test purposes this distribution was compared with

$$\Phi_{\tanh}(x, z; t = 0) = -W(z - h) \tanh [(z - h)/(z_0 - h)] \quad (\text{for } z \geqslant h), \tag{2.17}$$

and with

$$\Phi_{\arctan}(x, z; t = 0) = -(2/\pi)W(z - h) \arctan [(z - h)/(z_0 - h)] \quad (\text{for } z \geqslant h). \tag{2.18}$$

The differences were negligible and immaterial to the conclusions of this article, including neck distortion, jetting, tiny-bubble entrainment, and crown formation discussed in the next section. We also checked that the effect of β related to the initial configuration of the contact area is rather small (again, details in the next section). Similar tests were made by Oğuz & Prosperetti (1990) with a similar outcome.

3. Results, interpretation and discussion

As posed above, all the resuts in this section were obtained for axisymmetric flow, using cylindrical geometry. Accordingly, the radial coordinate x was restricted to positive values, but, for clarity, the plots are presented in a form containing symmetric negative values. The plots are to be understood as cross-sections containing the axis of symmetry. The x is then the coordinate in this cross-section perpendicular to the axis. In any case, all the results are symmetric with respect to the axis at $x = 0$.

In all the plots of this section showing the shape of the free surface, $z - H = 0$ indicates the unperturbed film level. The solid wall corresponds to $z = 0$, i.e. $z - H = -H$.

We consider an example from the series for the initial moments after impact with $W = 10$, $S = 1$ and $H = 0.25$, corresponding to an ethanol drop of $R = 1.7\,\text{mm}$ hitting an ethanol film of $h = 430\,\mu\text{m}$ with $w_0 = 1.3\ \text{m}\,\text{s}^{-1}$. We plot initial shape of the drop in figure 2. According to the initial condition (2.16) for the case shown in that figure we find that the horizontal velocity component $\text{D}x/\text{D}t$ is small (below 5%, of the order of 1% of the impact speed W) except near the neck, where it reaches values up to about double the speed of impact. For the vertical velocity $\text{D}z/\text{D}t$ we observe that the value on the sphere fluctuates by about 1% around its desired value of -10. Similarly, the values at the film surface far from the neck (where e.g. $x \geqslant 1$) are less than about 0.1% of the speed of impact. In the neck region itself, however, we observe changes of $\text{D}z/\text{D}t$ over a relatively large distance of a few tenths of the drop radius. Furthermore, the vertical velocity in the film region close to the neck is positive, indicating that fluid elements move upward there, away from the solid wall. In the same manner, the vertical velocity on the sphere close to the neck is larger than the impact speed, indicating that the fluid elements move faster towards the wall than the rest of the drop. The initial velocity distribution found by means of (2.16) plausibly represents the velocity field expected for the moment of impact of a drop moving against the z-axis at the velocity of $W = 10$.

3.1. *The initial moments after impact*

Let us consider in detail the behaviour of the neck. To this end, we resolve the small circle of radius r' by typically 10 nodes. For the set of parameters used in figure 2 we observe the formation of a jet-like structure in cross-section (see figure 3), which propagates into the free space between the impinging drop and the pre-existing liquid film.

In drop impact onto a liquid film at the wall, the velocity normal to the wall changes over the neck region from that of the impinging drop w_0, to zero at the

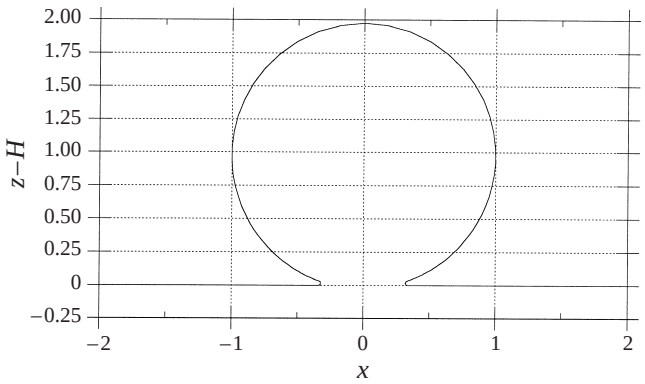

FIGURE 2. The initial surface shape for the case $W = 10$, $S = 1$, and $H = 0.25$. Thus, $We = 200$. $z - H = 0$ denotes the unperturbed film level, $z = 0$, i.e. $z - H = -H$, is the solid wall.

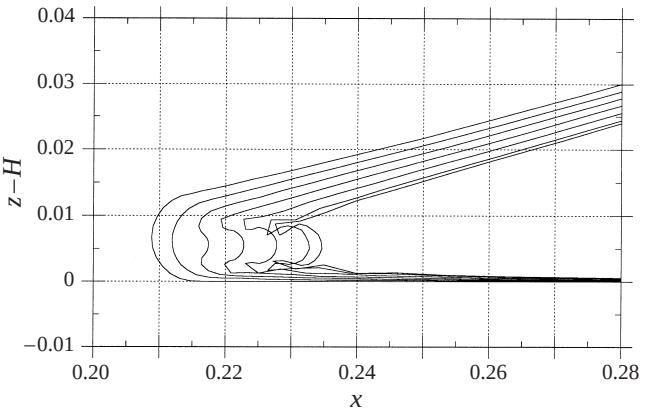

FIGURE 3. Evolution of the free surface in the case of $W = 10$, $S = 1$, and $H = 0.25$. Thus, $We = 200$. The different curves correspond from left to right to times 0, 1×10^{-4}, 2×10^{-4}, 3×10^{-4}, 4×10^{-4}, 5×10^{-4}, and 5.4×10^{-4}. The symmetry axis is at $x = 0$. We observe the formation of a jet-like structure in the cross-section, propagating into the free space between the impinging drop and the pre-existing liquid film. The structure reconnects with the film at about $t \approx 5.4 \times 10^{-4}$ after the impact, thereby trapping a torus-shaped volume of the surrounding gas.

impermeable wall. An almost step-like jump in velocity in an incompressible liquid with a free surface, when faster liquid particles push the slower ones (such as in the neck region in the present case), inevitably results in a liquid sheet outflowing normally to the free surface, if the velocity jump is large enough to allow the inertial forces to overcome the surface tension (Yarin & Weiss 1995). This fact is general and independent of any specific shape of the liquid domain, resulting, for example, in crown formation after a strong impact on a liquid layer (Levin & Hobbs 1971; Yarin & Weiss 1995; Cossali, Coghe & Marengo 1997). It also results in splashing bells on free liquid jets of relatively large radius with strong pulsations in the axial velocity imposed, for example, by a piston (see figure 7*c* in Meier, Klöpper & Grabitz 1992). For the same reason, jetting was encountered in the neck below a solid body entering an incompressible fluid (see figure 6 in Howison, Ockendon & Wilson 1991). Therefore, we conclude that the jetting corresponding to the relatively strong impact with $W = 10$ and $S = 1$ depicted in figure 3 is expected, and sets in inevitably, irrespective of any approximations involved in the initial smoothing of the neck zone.

In the example considered in figure 3, the jet reconnects with the film at about $t \approx 5.4 \times 10^{-4}$ (which corresponds with the parameters used above to 7μs) after the impact, thereby trapping a torus-shaped volume of the surrounding gas. It is clear that, at this stage, the simulation breaks down. This stems, first, from the topological change which takes place in the liquid volume, with the domain of the liquid considered forming holes, and its surface no longer connected; secondly, the tangential velocities at the sides of the reconnection section differ, in general, from each other, therefore a vorticity sheet is formed, which *a priori* can no longer be described by a scalar velocity potential only.

It is emphasized that the jetting depicted in figure 3 has nothing in common with the sideways jetting from the droplet bottom related to the formation of an expansion wave during the very early compressible stage of the impact (Lesser & Field 1983; Rein 1993). The former occurs in the middle of the neck region owing to the dominating inertial forces without any compressibility effects involved, and results in a free radial jet. By contrast, the latter sets in owing to the compressibility effects at the drop bottom, and results in a wall jet leading to formation of the contact area considered as an initial condition in the present work. Moreover, the experimental data of Field *et al.* (1989) show that jets resulting from the compressibility effects are actually not coherent. They are composed of a spray of secondary droplets which represent 'spalls' from the surface of the primary one. Also, in this case, the jetting velocity actually corresponds to the speed of propagation of the spallation front and thus is of the order of 10^3 m s^{-1}, whereas liquid particles move at a much lower speed, of the order of 10^2 m s^{-1} (Field *et al.* 1989).

The results shown in figure 3 allow us to estimate *a posteriori* the magnitude of the viscous effects. The latter could affect the flow via propagation of the shear wave from the wall or from the free surface (see e.g. Lundgren & Mansour 1988). For the flow duration $\Delta t_* = \Delta t(R/g)^{1/2}$ (Δt is dimensionless) the thickness of the liquid layer affected by the viscous effects may be estimated as $\delta_* \sim (\nu \Delta t_*)^{1/2}$, ν being the kinematic viscosity of the liquid. For free-jet-like structures such as those shown in figure 3, the viscous effects could affect the flow if the thickness Δ_* of such a jet is smaller than δ_*. Thus, for such structures, viscous effects could not be neglected if $\eta = \Delta_* g^{1/4}/(\nu^{1/2} R^{1/4} \Delta t^{1/2}) < 1$. For the jet-like structure of figure 3, we have $\Delta_* \sim 10^{-2} R$ and $\Delta t \sim 10^{-3}$. Thus, for $R = 1$ mm, $\nu = 1\text{mm}^2\,\text{s}^{-1}$ and $g \approx 10$ m s^{-2} we obtain $\eta \sim 10^{1/2}$ which shows that, in the present case, viscous effects cannot modify significantly even the flow in the tiny jetting region.

Viscous effects related to propagation of the shear wave from the free surface of the drop above the necking region are even less important, since there $\Delta_* \sim R$, and thus $\eta \sim 10^{5/2}$.

To estimate the effect of the shear wave propagating from the wall, we must take $\Delta_* \sim h$. In the case of figure 3, we have $h = 10^{-2} R$ and thus $\eta \sim 10^{1/2}$. Therefore, we conclude that the shear-related viscous effects near the wall can also be neglected.

Other cases considered below in the present subsection are even less restrictive than that of figure 3, so that the inviscid flow approximation is justified for all of them.

For a lower surface tension, the jet is thinner and faster (see figure 4, where the dimensionless surface tension is one-tenth of that of figure 3 with the other parameters fixed). It is still thicker, however, than without surface tension, cf. figure 5. Note that the leading part of the jet can under some circumstances (see e.g. figure 4) pinch off a part of its volume before it reconnects with the pre-existing film.

The jet formed at the neck can either reconnect with the film (see figure 3), or pinch off a part of its volume at the tip (see figure 4). In the former case, a torus-shaped

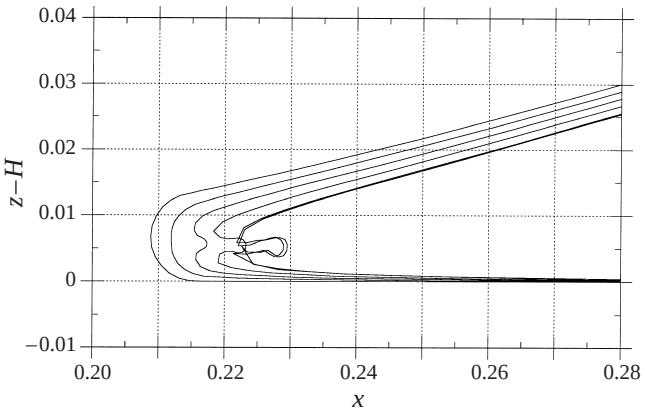

FIGURE 4. Evolution of the free surface in the case of $W = 10$, $S = 0.1$, and $H = 0.25$. Thus, $We = 2000$. The different curves correspond from left to right to times 0, 1×10^{-4}, 2×10^{-4}, 3×10^{-4}, 4×10^{-4}, and 4.1×10^{-4}. The leading part of the jet can, under certain circumstances, pinch off a part of its bulk before it reconnects with the pre-existing film.

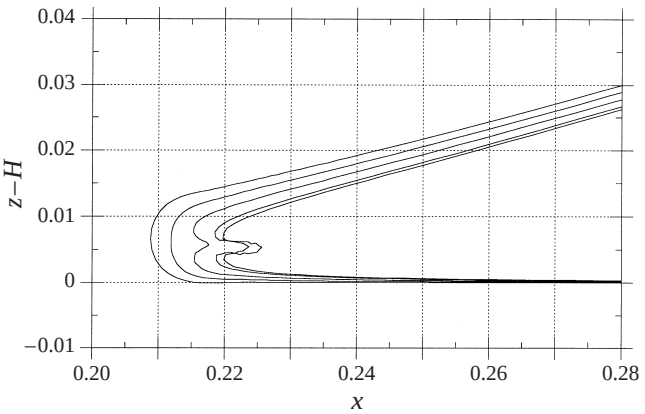

FIGURE 5. Evolution of the free surface in the case of $W = 10$, $S = 0$, and $H = 0.25$. Thus, $We = \infty$. The different curves correspond from left to right to the times 0, 1×10^{-4}, 2×10^{-4}, 3×10^{-4}, and 3.5×10^{-4}. The jetting cannot be attributed to capillary effects, which are totally excluded here.

bubble is entrained, whereas in the latter, a liquid torus is detached from the jet. Note that this mechanism leads to bubble entrainment even on shallow films. Both liquid torus and bubble will, in reality, decay according to Rayleigh's instability, thus spontaneously breaking the cylindrical symmetry assumed in the treatment here. This decay is associated with timescales comparable to the ones involved here, as can be seen in advance by dimensional analysis. Indeed, the most unstable mode of a cylindrical bubble grows as $\exp(\gamma_1 t)$, where the dimensionless growth rate γ_1 is, in our units, proportional to $(Sa_1^{-3})^{1/2}$, a_1 being the cross-section radius of the entrapped torus-shaped bubble. The numerical value for the proportionality factor is given, for example, by Chandrasekhar (1961), providing $\gamma_1 \approx 0.8201(Sa_1^{-3})^{1/2}$. With the typical value of $S = 1$, this leads to a timescale for this break-up of the order of $\gamma_1^{-1} \approx 1.22a_1^{3/2}$, which, in the example of figure 3, where $a_1 \approx 0.001$, is about 3.9×10^{-5}. This is comparable to, or shorter than the timescale of the jetting process in figure 3, which is of the order of 10^{-4} to 10^{-3}.

Consider also the case where pinch-off of the jet tip takes place, resulting in a liquid torus. The most unstable mode of a cylindrical liquid thread grows as exp ($\gamma_2 t$), where the dimensionless growth rate is $\gamma_2 \approx 0.3433(Sa_2^{-3})^{1/2}$ (Chandrasekhar 1961), a_2 being the cross-section radius of the thread. Taking, for example, figure 4, we estimate $a_2 \approx 0.002$. With $S = 1$, the characteristic timescale of the break-up becomes $\gamma_2^{-1} \approx 2.6 \times 10^{-4}$, which is of the order of 2.45×10^{-4}, i.e. the duration of the whole jetting process depicted in figure 4.

Therefore, for the results for the moments following the bubble entrainment or the pinch-off of the jet tip to become fully comparable with experiments – numerical simulations should be performed in three dimensions. At present, this is beyond the capacity of a work station, a personal computer and even a supercomputer, but in any case the three-dimensional structures (tiny bubbles and droplets resulting from break-up of the torus-like bubble and liquid torus, respectively) form at very early stages of the flow development. Indeed, their dimensionless timescale is 10^{-5} to 10^{-4}, which is very short compared to the overall development time, which is of the order of 10^{-1} to 1, as found below. These tiny bubbles and droplets are also very small in the scale of the flow itself. Indeed, in figure 3, the bubble volume is of the order of $2\pi \times 0.23 \times \pi \times 0.001^2 \approx 5 \times 10^{-6}$, whereas the initial drop has a volume of $\frac{4}{3}\pi \approx 4.189$. Such a bubble would quickly (see above for the timescale) decay into secondary bubbles with volumes of the order of $\pi \times 0.001^2 \times (2\pi \times 0.001/0.484)$ (see again Chandrasekhar 1961), which yields an equivalent radius of about 2×10^{-3} of the initial drop. Assuming R to be of the order of 1 mm, this yields us a secondary-bubble radius of the order of 2 μm, and even if these bubbles do not dissipate in the liquid, they may be difficult to observe. Micron-size bubbles are not readily amenable to detection in experiments at present, especially given the extremely short times of the order of 10^{-5} s involved. However, an experimental indication that such bubbles may, indeed, appear is elucidated by the photographs published by Chandra & Avedisian (1991). They were taken when drops impinged on a hot surface. In figure 6 in Chandra & Avedisian (1991), ten to fifteen bubbles are visible in a ring surrounding the centre of the drop impact. These bubbles were detected at temperatures below (and above) the boiling point and attributed to cavitation or nucleation at the nucleation sites on the heated wall. If that were the case, however, the bubbles should be distributed more or less uniformly and definitely not only in a ring-like region. On the other hand, according to the bubble encapsulation mechanism elucidated in the present work, a bubble ring should appear. We think that it became visible in the experiments of Chandra & Avedisian (1991) since liquid evaporation into the bubbles at elevated temperatures stabilized and enlarged them.

Estimate also the size of the droplets emerging from a liquid torus in the case of pinch-off of the jet tip, as depicted, for example, in figure 4. The ring breaks up rapidly (again see above for the timescale) into secondary droplets with volume of the order of $\pi \times 0.002^2 \times (2\pi \times 0.002/0.697)$ (see Chandrasekhar 1961), which yields an equivalent radius of about 3.8×10^{-3} of the initial drop. Thus, for $R = 1$ mm, the secondary droplets would have a radius of about 4 μm.

As a result, one can expect that these tiny bubbles and droplets will be rapidly smoothed, or at least will not affect substantially the overall flow development at the later stages.

Formation of the jet as illustrated in figure 3 cannot be attributed to surface tension effects. Indeed, the calculation for zero surface tension ($S = 0$) indicates jetting as well (see figure 5). Nor does it depend on the thickness of the pre-existing film, as is shown by figure 6. It is only very slightly affected by variation of the parameter

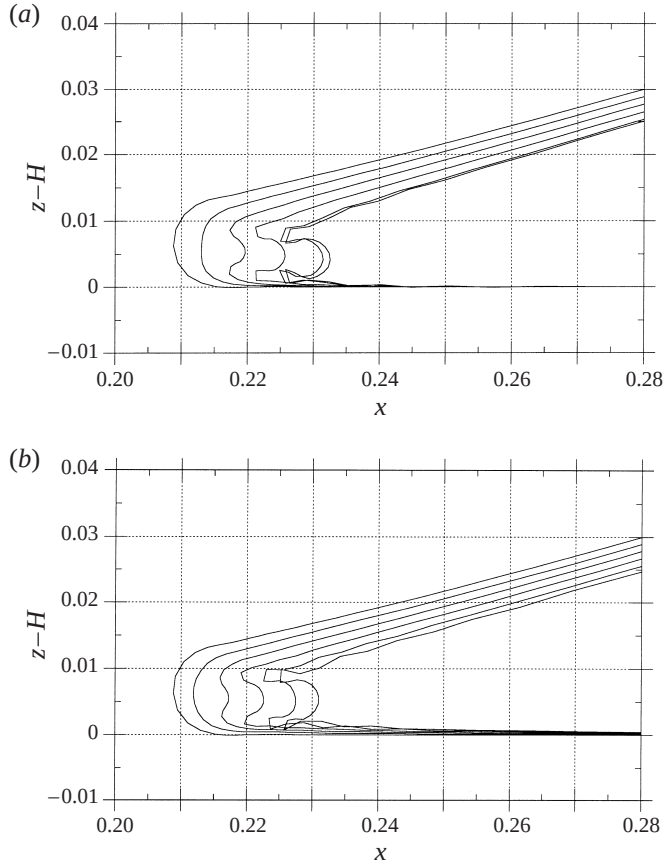

FIGURE 6. Evolution of the free surface in the case of (*a*) $W = 10$, $S = 1$, and $H = 0.01$, (*b*) $W = 10$, $S = 1$, and $H = 2.25$. Thus, $We = 200$. In (*a*), the curves correspond from left to right to times 0, 1×10^{-4}, 2×10^{-4}, 3×10^{-4}, 4×10^{-4}, and 4.2×10^{-4}. In (*b*), the curves correspond from left to right to times 0, 1×10^{-4}, 2×10^{-4}, 3×10^{-4}, 4×10^{-4}, and 4.7×10^{-4}. Formation of the jet is independent of the thickness of the pre-existing liquid film. The jetting sets in and evolves practically on the same timescale and takes very similar spatial shapes.

β responsible for the initial contact area (see § 2). In figure 6(*a*), jetting at $W = 10$, $S = 1$ and $H = 0.01$ was predicted with $\beta = 0.99$, and bubble encapsulation occurs at about $t = 4.2 \times 10^{-4}$. A similar scenario was also concluded for $\beta = 0.95$, 0.995 and 0.998 with encapsulation times of about 5×10^{-4}. Thus, we can state that, at different values of β, only some minor details change but the phenomena are similar.

On the other hand, jetting depends crucially on the impact velocity; in fact, it does not set in when the latter is low enough (see figure 7); for the ethanol drop mentioned above, this corresponds to $w_0 = 0.13$ m s^{-1}. Instead, the whole neck region moves outwards under the action of surface tension, and capillary waves begin to propagate outwards as well. The surface tension always tends to damp the jetting. Accordingly, dominance of the surface-tension effects over the inertial ones, as in figure 7, precludes formation of fine structures such as jetting, since the latter leads to increase of the surface energy. At intermediate values of the surface tension, an intermediate scenario between motion of the whole neck region and formation of a jet occurs; jetting proceeds against the background of developing motion of the whole neck.

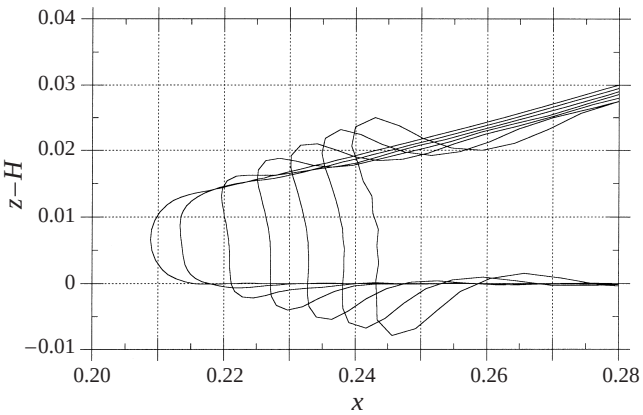

FIGURE 7. Evolution of the free surface in the case of $W = 1$, $S = 1$, and $H = 0.25$. Thus, $We = 2$. The different curves correspond from left to right to times 0, 5×10^{-4}, 10×10^{-4}, 15×10^{-4}, 20×10^{-4}, 25×10^{-4}, and 30×10^{-4}. The jet does not arise since the impact speed is low enough. Instead, the whole neck region moves outwards under the action of the surface tension.

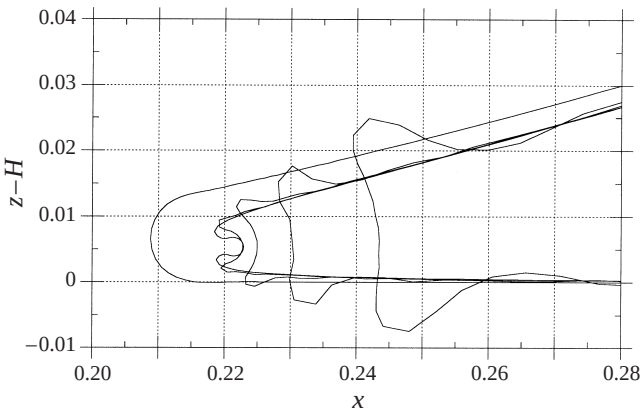

FIGURE 8. The effect of surface tension. The plot shows the free surface shape for $W = 10$, $H = 0.25$, and for several values of the dimensionless surface tension S at time $t = 0.0003$ after impact. The first curve on the left represents the initial shape. The remaining curves correspond from right to left to the dimensionless surface tensions $S = 100$, 20, 5, 1, and 0.2, in turn corresponding to $We = 2$, 10, 40, 200, and 1000, respectively.

We summarize the influence of the surface tension on jet formation in figure 8. It is obvious that jetting occurs at the limit of relatively weak surface tension (relative to the inertial effects), whereas sufficiently strong surface tension is able to suppress it. The reason for the latter is that negative pressure may arise in the neck region owing to very large curvature in the axial cross-section ($p \sim -\alpha|\partial^2 x/\partial s^2|$). This negative pressure actually corresponds to outward stretching of the liquid in the whole neck by surface tension forces. This effect overcomes the jetting in the middle part and leads to the scenario shown, for example, in figure 7. Note that these negative pressures are in practice still small compared to the atmospheric pressure, so that cavitation does not occur in practice in the bulk of the liquid.

The motion of the neck outwards without jetting, and the accompanying capillary waves at the very first moment of a weak impact, look very similar to those found by Oğuz & Prosperetti (1989). Note, however, that the opposite volumes of liquid never

Label	W	S	H	We	Phenomenon	u_{jet} or u_{neck}	$V_\alpha = [2\alpha/(\rho\delta)]^{1/2}/(Rg)^{1/2}$
1	20	1	0.25	800	Jetting	100	12
2	10	1	0.01	200	Jetting	66	12
3	10	0	0.25	∞	Jetting	66	0
4	10	2	12.25	100	Jetting	58	17
5	10	100	0.25	2	Whole neck moving outwards	120	122
6	1	1	0.25	2	Whole neck moving outwards	12	12

TABLE 1. Comparison of the impact speed W, and the jet tip velocity u_{jet} or the neck velocity u_{neck}, respectively, with the velocity $V_\alpha = (2\alpha/\rho\delta)^{1/2}/(Rg)^{1/2}$. The velocity u_{jet} or u_{neck} is taken at time $t = 2 \times 10^{-4}$ in cases 1–5 and at $t = 2 \times 10^{-3}$ in case 6. We note that the respective velocities of the jet tip and neck are significantly higher than the impact speed.

touched each other in our simulations of a weak impact, as was the case in the former work. We attribute this difference to the geometry of the situation, i.e. the effect of the sphere.

To analyse the initial flow development in the neck region, we consider the horizontal velocity of the jet tip or the whole neck moving outwards. For that of the jet tip we take the value of $\mathrm{D}x/\mathrm{D}t$ at a site where $\partial x/\partial s = 0$ and $\partial^2 x/\partial s^2 < 0$. There are actually two such sites: one in the neck region, the other near the drop equator. Obviously, we consider the one in the neck region. For the velocity of the neck, we take $\mathrm{D}x/\mathrm{D}t$ at the site where $\mathrm{D}z/\mathrm{D}t = 0$. ($\mathrm{D}z/\mathrm{D}t \approx 0$ also throughout the whole liquid film far from the neck.) These velocities are plotted for some cases in figure 9 as functions of time, with which they evidently vary. In particular, it is observed that they are in all cases significantly higher than the impact speed, cf. table 1, where the velocities u_{jet} and u_{neck} corresponding to $t = 2 \times 10^{-4}$ (cases 1 to 5) and $t = 2 \times 10^{-3}$ (case 6) are presented. In table 1 we also give the dimensionless speed $V_\alpha = [2\alpha/(\rho\delta)]^{1/2}/(Rg)^{1/2}$ (cf. our velocity unit introduced in § 2), which from dimensional analysis should provide a meaningful velocity scale in this context. The lengthscale δ involved in V_α is of the order of the gap width near the neck. Thus, for δ/R we have put the neck width as $2r', r'$ again being the radius of the tiny circular arc serving as an initial neck region under the impinging drop, rendered dimensionless by R. From table 1, we conclude that a jet driven by inertial effects can arise at the neck if it is sufficiently fast to outrun the outward motion of the whole neck with a velocity of the order of V_α, or in other words, if surface tension is too weak to accelerate the fluid parts situated at the neck. So, it is evident that the jetting corresponds to inertial effects dominant over those due to surface tension.

In the first line of table 1, the jetting velocity is 5 times that of the impact. Taking $w_0 = 1\,\mathrm{m\,s^{-1}}$ we thus estimate the jetting velocity as $5\,\mathrm{m\,s^{-1}}$.

Based on the findings in table 1 about the relation between W and u_{jet}, we conclude that the jet tip velocity u_{jet} (if jetting actually occurs) scales roughly with the speed of impact W, i.e. $u_{jet} = K(t)W$, where K is a function of time with values of the order of several units (according to figure 9 and table 1). We obtain then, for the ratio between the jet tip velocity and the speed V_α, the expression $u_{jet}/V_\alpha = KW(Rg)^{1/2}/(\alpha/[\rho R r'])^{1/2} = K(We/2r')^{1/2} = K(\frac{1}{2}We)^{1/2}r'^{1/2} = KWe_{neck}^{1/2}$. Therefore, the ratio u_{jet}/V_α yields up to a factor the square root of $We_{neck} = \rho r' R w_0^2/\alpha$, a Weber number based on the neck width rather than on the drop radius. Thus, the condition $u_{jet}/V_\alpha \gg 1$ is equivalent to $K(We_{neck})^{1/2} \gg 1$, which yields $We_{neck} = (\frac{1}{2}We)r' \gg 1/K^2$ for jetting. The latter essentially means $We_{neck} \gtrsim 1$ for jetting.

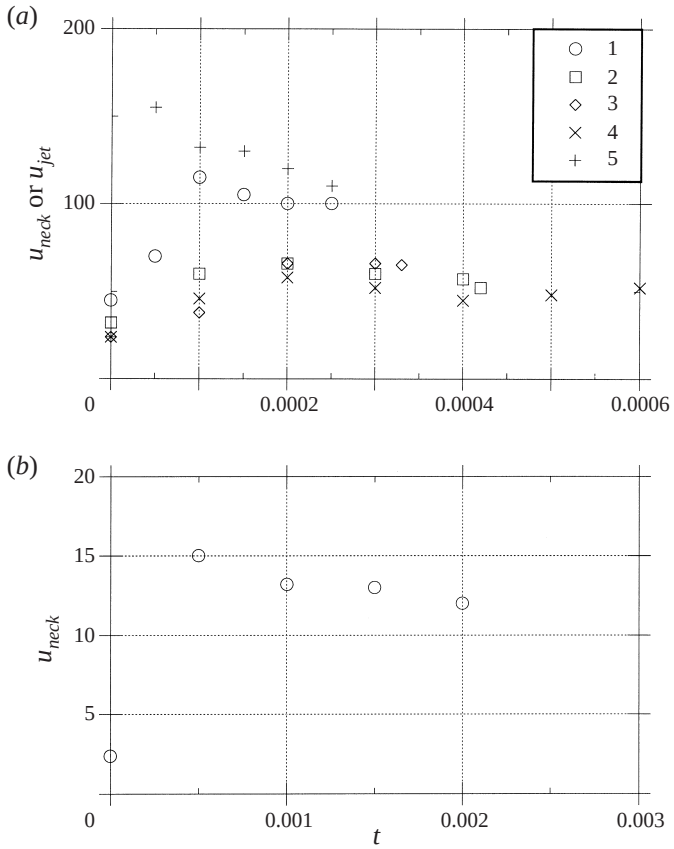

FIGURE 9. The velocity of the jet tip u_{jet} (in the case of jetting) and that of the neck centre u_{neck} (in the case where the whole neck moves outwards accompanied by capillary waves) as functions of time. The numerals 1 to 5 labelling the different cases in (*a*) are the same as in table 1; (*b*) shows the data for case 6 of table 1. Note that in all the cases the velocities reach values significantly higher than the impact speed W. Note the different timescales for (*a*) and (*b*).

From our numerical results, we also observed that the critical value $We_c^{(jetting)}$ of We corresponding to the onset of jetting varies essentially as $1/r'$. In figure 8, $We_c^{(jetting)} \approx 40$, and since $r' = 1/150$ there, we obtain approximately $We_c^{(jetting)} \approx 4/(15r')$. As shown below, the value of $r' = 1/150$ is given by physical arguments.

Thus, our findings can be summarized by the statement that jetting occurs if $We \gg We_c^{(jetting)} \approx 40$, and that capillary waves occur instead if $We \ll We_c^{(jetting)}$. This is indeed the case , as the values of We in table 1 show.

The question remains finally what happens if r' is varied, in particular shifted towards zero. At first glance, one would expect that $We_c^{(jetting)}$ grows to infinity, i.e. that jetting does not occur, if only r' is taken sufficiently small. Note, however, that, in physical situations, r' cannot decrease below any limit, and in practice there is a lower bound for it. Indeed, first of all at the very short initial compressible stage (see § 2) a finite contact zone appears at the bottom of the drop, of the order of $r_c = Rw_0/c_0 \sim 1$ μm. This zone includes an area where the drop surface merges with the liquid layer on the wall. The radius of curvature of the merging zone is very small, and a plausible approximation is to assume that it is zero (see e.g. Keller & Miksis 1983). Smoothing of the acute corner by surface tension proceeds with the

velocity $v \approx (\alpha/[\rho t])^{1/3}$ (due to the dimensions of the parameters involved). At $t = 0$, $v = \infty$. This is, however, an integrable singularity, and does not lead to instantaneous smoothing of a zone of the order of r_0. Indeed

$$r_0 = \int_0^{t_0} v\,\mathrm{d}t = \tfrac{3}{2}(\alpha t_0^2/\rho)^{1/3}.$$

Thus $r' \sim r_0/R = \frac{3}{2}(\alpha t_0^2/[\rho R^3])^{1/3} = \frac{3}{2}(S t_0'^2)^{1/3}$, where $t_0' = t_0/(R/g)^{1/2}$. The onset of jetting corresponds to $t_0' \approx 10^{-4}$ to 10^{-3} for $S = 1$ according to the results of figure 3. Thus, at the beginning of the jetting process $r' \sim \frac{3}{2} \times 10^{-8/3}$ to $\frac{3}{2} \times 10^{-2}$, but not less than that. In our calculation, it was accordingly $r' = \frac{1}{150}$. So we can say that compressibility effects and then surface tension first form a (circular) arc over the neck and only then does jetting (and our simulation) begin.

Note also that the effect of the dispersion (London) interaction of the liquid molecules and the wall (Zimon 1982) is less important in the given case than that of the surface tension considered above. Indeed, for the smoothing due to the dispersion interaction $v \approx (A/[\rho t^3])^{1/5}$, where A is the Hamaker–van der Waals constant. Thus $r' \sim \frac{5}{2}[(A/[\rho R^4 g])t_0'^2]^{1/5}$. Given $A \approx 10^{-20}$ J, $\rho = 1000\,\mathrm{kg\,m^{-3}}$ and $R \approx 1$ mm, we obtain $r' \sim \frac{5}{2} \times 10^{-4}$ to $\frac{5}{2} \times 10^{-18/5}$ for $t_0' \approx 10^{-4}$ to 10^{-3}. Comparing with the values of r' resulting from the effect of surface tension, we conclude that the latter is dominating.

Pumphrey & Elmore (1990) described several scenarios of bubble entrainment in deep liquids. Some of them were explained theoretically. Another scenario, the 'Mesler entrainment', experimentally observed in Esmailizadeh & Mesler (1986), was discussed in Oğuz & Prosperetti (1989) and found to be compatible with their numerical results. One of the features arising in the Mesler entrainment fits also, to a large extent, with what we would expect as an experimental manifestation of our simulations. Indeed, this kind of entrainment traps a very large number of tiny bubbles formed near the neck, if the drop impacts on a deep liquid layer. Mesler entrainment was observed only at moderate-impact Weber numbers, however, and is replaced or masked by other mechanisms at higher Weber numbers in the case of deep liquids. From figure 5 in Pumphrey & Elmore (1990), obtained for water, we can see that the parameters leading to Mesler entrainment with the largest Weber number are $d \approx 1$ mm for the drop diameter and $v \approx 3\,\mathrm{m\,s^{-1}}$ for the impact velocity, i.e. $R \approx 0.5$ mm and $w_0 \approx 3\,\mathrm{m\,s^{-1}}$ in our notations. For water, this corresponds to $We \approx 125$ or $S \approx 29$ and $W \approx 43$. On the other hand, our simulations for a relatively thick pre-existing liquid film predict an intermediate behaviour in the case of $We = 100$; the jet begins to develop against the background of motion of the whole neck. They show entrainment of tiny bubbles at higher impact Weber numbers ($We \gtrsim 200$), and the higher the better, which does not correspond to Mesler entrainment. It is not clear whether Mesler's scenario can also be observed on shallow liquid films, as is predicted by our simulations; so far, it has been observed on deep pools only. For low-Weber-number impact, our simulations do not predict bubble entrainment. As an example, we take a water drop with $d \approx 1$ mm and $v \approx 0.85\,\mathrm{m\,s^{-1}}$ i.e. $R \approx 0.5$ mm and $w_0 \approx 0.85\,\mathrm{m\,s^{-1}}$, thus $We = 10$, $S \approx 29$ and $W \approx 12$. According to Pumphrey & Elmore's figure 5, this should lead to Mesler entrainment (on deep liquids), whereas our simulations predict the neck moving outwards as a whole without any bubbles formed, see the curve with $S = 20$ in our figure 8. Therefore, we think that these numerical results manifest a mechanism of bubble entrainment different from that of Mesler. Our mechanism actually replaces Pumphrey & Elmore's regular and irregular mechanisms

for relatively high-speed impacts, which cannot proceed in the shallow-liquid case; instead of them, we find formation of tiny bubbles trapped by the jetting.

Note finally that Oğuz & Prosperetti (1989, 1990) did not observe any jetting at the neck, as we did in the case of a strong impact. In the first work, a liquid neck between two infinite liquid masses was considered. At zero collision velocity, they found evolution of the free surface rather similar to that of our figure 7, which is characteristic of weak impacts. On the other hand, direct comparison of our results with the former with non-zero collision velocity is impossible, since they considered infinite liquid masses, and thus no droplet radius can be defined, which rules out confrontation of our dimensionless governing parameters W and S with theirs. Only the criterion using the neck-based Weber number can be used. Our We_{neck} corresponds to their U_*^2. In their cases, $U_*^2 \leqslant 1$. As shown above, $We_{neck} \gtrsim 1$ for jetting. Thus, the criterion for jetting we described above is not fulfilled in Oğuz & Prosperetti (1989). In the second work, two cases of drop impact on a liquid surface were computed; they correspond to (i) $W = 11.2$ and $S = 2.035$, which yields $We = 123$, and (ii) $W = 14.2$ and $S = 0.87$, which yields $We = 466$. In both cases, $H = \infty$. It is not clear whether this work provided sufficiently fine resolution of the neck region to be able to observe jetting. If so, the fact that the liquid layer was actually infinitely deep, allowing for development of vertical flow, may be responsible for the absence of jetting in their calculations. Furthermore, they included an artificial curvature damping in their numerical code, which might suppress such small-scale details as jetting.

3.2. *Results for large times after impact*

In this subsection, we do not consider the part of the neck in minute detail. We therefore place very few nodes on the small circular arc corresponding to the neck at the initial moment, typically only one or two. As a result, the initial jetting and subsequent reconnection are smoothed out. We have seen in § 3.1 that the entrapped torus-shaped bubble disintegrates quickly into tiny bubbles. We postulate that neither these bubbles nor the shear layers resulting from the reconnection affect substantially the overall behaviour of the impinging and spreading drop and crown formation, and therefore we smooth them out here.

As a first example, we take the case of a thin pre-existing liquid film. Initially, one would tend to assume that this case is close to that of impact onto a dry wall. This approach, however, does not allow for the effects of wall roughness and wettability, which may prove crucial in practical situations. Thus, we assume implicitly that the wall is ideally smooth and always covered by the film.

In figure 10, we show the free surface of the liquid volume for several moments after drop impact. The shapes shown in figure 10 should be considered as a continuation of the scenario illustrated in figure 6(*a*) at timescales 10^3 times that of the latter. One observes the formation of a crown, which propagates outwards away from the axis of impact along the solid wall. This phenomenon has frequently been observed experimentally, beginning with Worthington (1876, 1877), and identified as the effect of a kinematic discontinuity in the spreading lamella (Yarin & Weiss 1995). Furthermore, it has been found that the effect is suppressed by sufficiently strong surface tension. To check this, we consider the same problem with increased dimensionless surface tension, $S = 10$. The result is shown in figure 11. The difference in behaviour is evident: practically no crown is formed, and the drop gradually spreads over the wall. This pattern is similar to those found numerically for droplet spreading by Fukai *et al.* (1993, 1995), Hatta *et al.* (1995) and Pasandideh-Fard *et al.* (1996). By contrast, the pattern of figure 10 is totally different: to the best of our knowledge, it represents

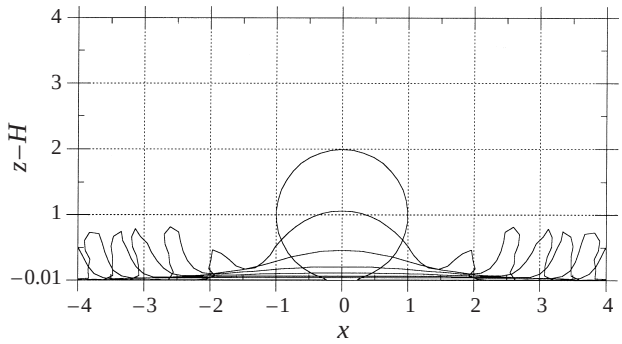

FIGURE 10. Crown formation. Evolution of the free surface in the case $W = 10$, $S = 1$, and $H = 0.01$. Thus, $We = 200$. The different curves correspond to times 0, 0.1, 0.2, 0.3, 0.4, 0.5, and 0.6. The formation of a crown can be observed. The crown propagates outwards away from the axis of impact along the solid wall. In this, and the following calculations, the initial neck region is not resolved in fine detail. As a result, the initial jetting and reconnection are smoothed out.

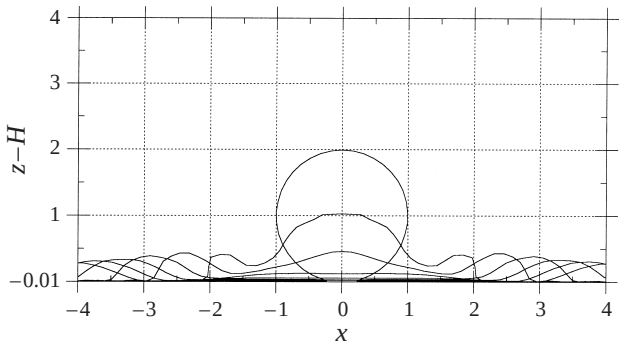

FIGURE 11. Drop spreading. Evolution of the free surface in the case $W = 10$, $S = 10$, and $H = 0.01$. Thus, $We = 20$. The different curves correspond to times 0, 0.1, 0.2, 0.3, 0.4, 0.5, and 0.6. There is practically no crown formed, since the inertial effects are relatively weak compared to the capillary ones. As a result, the drop gradually spreads over the wall.

the first BEM-based two-dimensional numerical simulation of crown formation and propagation.

The characteristic time of the drop-splashing process shown in figure 10 is $\Delta t \sim 10^{-1}$. Estimating first the viscous effects from the free surface of the drop, we take $\Delta_* \sim R$ and obtain $\eta \sim 10^{3/2}$ (v and R being the same as in § 3.1). Thus, the viscous effects associated with the shear near the free surface can be neglected.

For the viscous effects associated with the shear from the wall we take $\Delta_* \sim h = 10^{-2} \times R$ and thus $\eta \sim 10^{-1/2}$. In this case the viscous forces can damp the liquid film on the wall during propagation of the crown, as discussed by Yarin & Weiss (1995). However, since the crown mass is much larger than that of the affected near-wall bottom zone, the overall effect of the damping on the predominantly inertial crown propagation will still be insignificant at times of the order of several Δt. The latter enables us to believe that the potential flow of figure 10 represents accurately the pattern of the real viscous flow.

Other cases considered in the present section are even less restrictive with regard to the viscous effects.

In the experiments of Shin & McMahon (1990) with drop impact on liquid layers, formation of the Worthington jets rising from the middle of the crater was found for

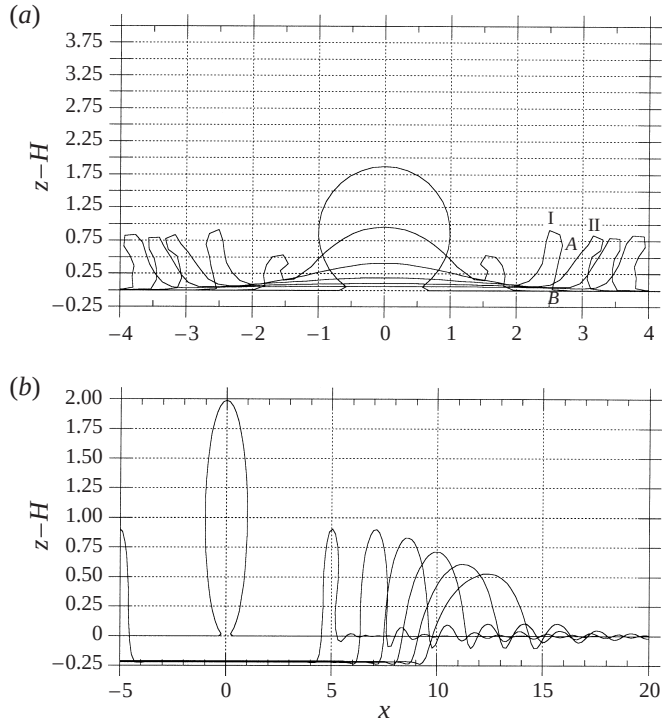

FIGURE 12. Evolution of the free surface in the case $W = 10$, $S = 1$, $H = 0.25$. Thus, $We = 200$. (*a*) The different curves correspond to times 0, 0.1, 0.2, 0.3, 0.4, and 0.5. At the beginning, the crown is tilted backwards towards the drop. It straightens and tilts forward later at about $t = 0.2$. (*b*) The different curves correspond to times 0, 1, 2, 3, 4, 5 and 6. The crown is preceded by capillary waves. The film thickness behind the crown is smaller than that of the unperturbed film. Note the contracted x-axis in (*b*), which makes a spherical drop take a cigar-like shape in the plot.

depths of the order of the crater radius. On the other hand, the results of figure 10 do not show any sign of Worthington jetting. The reason for the latter is as follows. The crater radius in the target liquid (if a crater appears) is at least larger than that of the incident drop. The depth in the case of figure 10 is $H = h/R = 0.01$. When the depth of the liquid layer was smaller than the crater radius, Shin & McMahon (1990) did not find any Worthington jetting, just as we do not find it in the present work dealing only with very shallow liquid layers. In another case considered below in the present subsection (figure 12), $H = h/R = 0.25$, and Worthington jetting does not appear either.

Let us now consider the influence of the film thickness. For that purpose, we take first a case with $H = 0.25$. The results are shown in figure 12. We observe that a crown forms largely as in the case $H = 0.01$. As before, it deviates slightly from the normal to the wall and propagates outwards from the z-axis. At the beginning it is tilted backwards at its top, subsequently it becomes almost straight and finally tilts forward. Furthermore, it is evident that the film thickness behind the crown is smaller than the original one (see figure 12(*b*) where the x-axis is contracted, thus making a spherical drop look cigar-like), which means that the liquid combined in the crown stems partly from the film itself. This is also true for the case with $H = 0.01$, but of course much less obvious. It is in agreement with the prediction based on our model developed and published earlier (Yarin & Weiss 1995). The detailed behaviour of the

film thickness behind the crown as a function of time is not very conclusive, however, since the thickness is very small at large times, and even small numerical inaccuracies acquire weight.

For very thin initial films, for example, such as that corresponding to figure 10 ($H = 0.01$), the crown mainly consists of the liquid from the drop for $t = O(1)$. Therefore, at $0.2 \leqslant t \leqslant 0.6$, when a fully developed crown already exists and propagates outwards, its volume may be expected to be approximately constant. Numerically, the crown volume does not change more than by a few percent over this interval. Thus, the product of an effective crown thickness Δx times its height Δz should be proportional to $x^{-1}, \Delta x \Delta z \sim x^{-1}$. The numerical results in figure 10 show that Δz is approximately constant at $0.2 \leqslant t \leqslant 0.6$. The effective thickness of the crown Δx slightly decreases as x^{-1} from $x \approx 2.5$ to 3.5. At later times, an increase in the crown volume is more pronounced owing to accumulation of the liquid scraped from the film in front of the crown and sucked from the film behind it.

In figure 12(*b*), we plot the behaviour for relatively large times after the impact. It can be observed that the crown is preceded by capillary waves on the film. We have already observed this feature in our quasi-one-dimensional simulations (Yarin & Weiss 1995), and it can also be observed in experiments (Edgerton and Killian, as reproduced in Peregrine, Shoker & Symon 1990).

Also, for a still thicker film with $H = 1$, the results of our simulations show that the crown in the beginning consists mainly of the liquid of the drop, and only later also scrapes a significant mass from the pre-existing liquid film. Note also that, in the case of that film, the inner side of the crown becomes steeper and steeper, until $\partial x/\partial s$ becomes negative. This may eventually lead to entrainment of a bubble inside the crater, as described by Oğuz & Prosperetti (1990).

At smaller impact velocities (e.g. $W = 2$ and 5 instead of $W = 10$ of figures 10 and 12) the crown practically disappears.

Let us now compare the results for large times after impact with our previous quasi-one-dimensional model (Yarin & Weiss 1995), hereinafter referred to as the YWM.

The YWM is relevant for the impact of drops impinging one by one on a solid wall. In this case, a liquid film of thickness $h_0 \approx (\nu/f)^{1/2}$ is damped on the wall by the viscous forces (ν is the kinematic viscosity, and f the frequency of the drop train) and the oncoming drops impinge on this film. The YWM made use of the dimensionless parameter $\varepsilon = \alpha h_0 f^2/(\rho w_0^4)$ (i.e. the ratio of the surface tension forces to the inertial ones). According to the YWM, a crown emerges only for small ε when the impact velocity is high enough and inertial forces dominate. Otherwise, capillary waves propagate from the point of impact.

A similar pattern is found in the present numerical simulations for a single drop impact. The results of the present work show emergence of a crown propagating over the film along the solid wall, if the impact velocity is high enough. If surface tension is strong enough, we do not observe any crown but only the spreading of a drop accompanied by capillary waves.

A more detailed and quantitative comparison of crown formation and the splashing threshold in the two cases of drop impact (i.e. a drop train onto an initially dry wall – which is covered afterwards by a liquid film stemming from the preceding drops – on one side, versus a single drop on a liquid film on the wall on the other side) is delicate. In the first case, the frequency f is given, whereas the thickness of the liquid film damped by viscous forces on the wall depends on it as $h_0 \approx (\nu/f)^{1/2}$. In the second case, the thickness h (as it is denoted in the present work) of the film

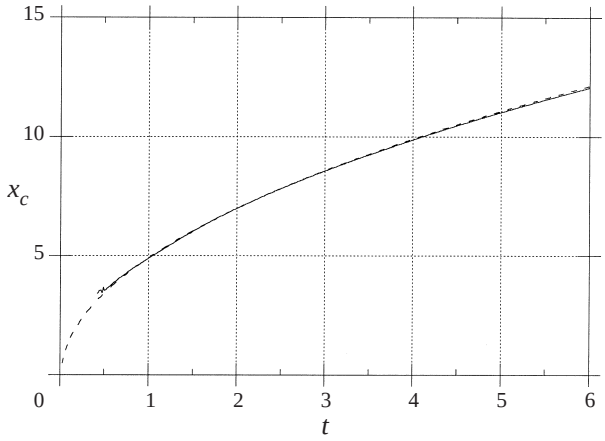

FIGURE 13. The kinematics of the crown spreading over the liquid film along a solid wall. The parameters are those of figure 12. ——, crown radius as a function of time; — — —, best fit to it of the form $x_c = [C\,(t - t_0)]^{1/2}$, where $C = 24.7$ and $C\,t_0 = 0.5$, i.e. $t_0 = 0.020$.

on the wall is given. Thus, the situations are different and their comparison is not straightforward. Yarin & Weiss (1995), however, showed that if h_0 is replaced by $(v/f)^{1/2}$ and the frequency f formally replaced by $w_0/(2R)$, the results of the YWM coincide with those of Stow & Hadfield (1981) found experimentally for a threshold of crown formation and splashing for single-drop impact. They also showed that similar substitution permits prediction of the rate of crown propagation in the case of a single-drop impact on a liquid layer studied experimentally by Levin & Hobbs (1971). Cossali *et al.* (1997) in their experimental study of a single-drop impact on a thin liquid film also confirmed the above substitution and showed that the predictions of the YWM, with the characteristic frequency of $w_0/(2R)$, correctly describe their data.

Expressed in terms of the dimensionless groups used here, $\varepsilon \approx \frac{1}{4}SHW^{-2} = H/(2We)$. For the data of figure 10, the value of the parameter $U = \varepsilon^{-1/4}$, also used in the YWM, is $U \approx 14$, which is close to that of $U \approx 18$, corresponding to formation of secondary droplets at the crown top (splashing) according to Yarin & Weiss (1995).

The critical value for crown formation $We_c^{(crown)}$ for $H = 0.25$ is of the order of 100, while that for jetting $We_c^{(jetting)}$ found for $H = 0.25$ in figure 8 is about 40. Thus, the parameter ranges producing a transition regime with respect to formation of a jet and a crown, respectively, are rather close to each other. As a result, a flow producing jetting at the very beginning will then result in crown formation.

We consider now the asymptotic behaviour of the crown radius as a function of time. We take the example shown in figure 12 and find the result plotted in figure 13. The crown radius can be very accurately described by a square-root function of time: $x_c = [C(t - t_0)]^{1/2}$, where $C = 24.7$ and $Ct_0 = 0.5$, i.e. $t_0 = 0.020$. This square-root dependence was predicted and verified experimentally in Yarin & Weiss (1995), and is also supported by the experimental data of Cossali *et al.* (1997).

To compare the numerical results in more detail with the predictions of the YWM, we consider the velocity distribution $\mathrm{D}x/\mathrm{D}t$ at time $t = 0.2$ after impact (see figure 14). At this moment, the drop has nearly merged with the film, its apex is at $z - H \approx 0.4$. The crown has formed (I in figure 12*a*), is situated at $x_c \approx 2.4$ and already tilted

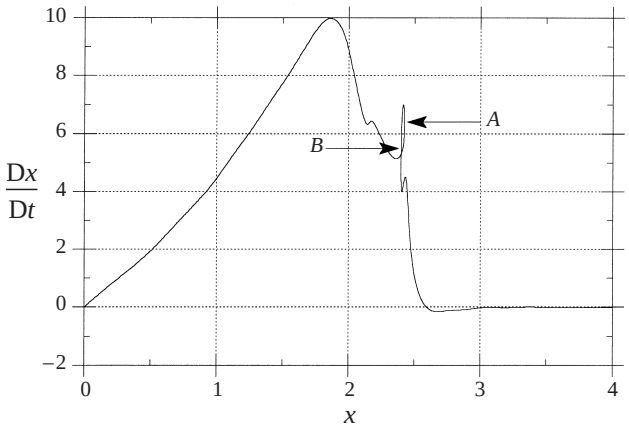

FIGURE 14. The velocity distribution $\mathrm{D}x/\mathrm{D}t$ at $t = 0.2$ after impact. The parameters are those of figure 12. The drop has nearly coalesced with the film. The crown has formed and is already tilted forward. This leads to the discontinuity in $\mathrm{D}x/\mathrm{D}t\,(x)$ at about $x_c = 2.4$, where the crown is situated at this instant. By integrating $\mathrm{D}x/\mathrm{D}t$ over x, we numerically obtain 12.51 which is in very good agreement with the value 12.35 predicted by the YWM based on the findings from figure 13.

forward. The crown manifests itself as a steep drop of velocity $\mathrm{D}x/\mathrm{D}t$ at $x_c \approx 2.4$. Note the very narrow loop in the velocity distribution in figure 14. It refers to sites A and B of crown I and means that point A (corresponding roughly to the rim of the crown) moves outwards slightly faster than B (corresponding roughly to the 'root' of the crown). Indeed, crown II next shown in figure 12(a) is tilted forward more than crown I.

According to the YWM, integration of the horizontal component of the surface velocity $\mathrm{D}x/\mathrm{D}t$ over x yields the value of $\frac{1}{2}C$. Figure 14 yields numerically $\frac{1}{2}C \approx 12.51$, thus $C \approx 25.02$, which is in very good agreement with the value of $C \approx 24.7$ found above. Thus, the kinematic predictions of the YWM are fully supported by the present numerical results.

We now compare our results with experimental findings and other numerical results from literature. As mentioned before, the crown has been widely observed and reported on, for example, in the experimental studies of Worthington (1876, 1877), Levin & Hobbs (1971), Stow & Hadfield (1981), Yarin & Weiss (1995), and Cossali *et al.* (1997). This aspect of our numerical results is thus in agreement with other works.

Experiments of Levin & Hobbs (1971) and Yarin & Weiss (1995) demonstrated also the formation of a free rim on the top of the crown owing to the action of surface tension. As was explained in the latter work, cusps are formed on this rim, leading to formation of secondary droplets on the top of the crown. The spatial resolution of the present numerical simulations is not high enough to bring out the details of the rim, although the crown shapes in figures 10 and 12 at $t = 0.5$ do hint at a free rim. The present method, confined to axisymmetric shapes, is definitely incapable of describing such three-dimensional phenomena as the cusp formation mentioned above.

Our numerical results show, in the case of film thickness $H = 0.01$ with crown formation absent, that the front of the spreading lamella is nevertheless thickened (see figure 11). This is due to the effect of surface tension, counteracting the spreading which results in a rim. It is in agreement with experimental and numerical evidence by Chandra & Avedisian (1991), Fukai *et al.* (1993, 1995), Hatta *et al.* (1995) and Pasandideh-Fard *et al.* (1996).

4. Summary and concluding remarks

We can summarize the findings in the present work as follows:

(i) In the case of a relatively strong impact of a single drop on a liquid layer at the wall, at $We \gg 40$ (e.g. $We \gtrsim 200$) jetting sets in in the middle of the neck between the oncoming drop and the liquid layer.

(ii) The tip of the jet may reconnect with the free surface of the liquid film at the wall, thereby trapping a torus-like bubble.

(iii) On the other hand, the tip of the jet may also pinch off before the reconnection, thereby producing a liquid torus.

(iv) The torus-like bubble breaks up rapidly (typically at about $t \approx 3.9\times10^{-5}(R/g)^{1/2}$ after formation) into a number of tiny bubbles with equivalent radius of about 2×10^{-3} times the initial drop radius R (g being acceleration due to gravity).

(v) The liquid torus pinched off from the jet tip also breaks up rapidly, typically at about $2.6 \times 10^{-4}(R/g)^{1/2}$ after formation, into a number of tiny droplets with equivalent radius of about $3.8 \times 10^{-3}R$.

(vi) The phenomena described in (iv) and (v) lead to a developed three-dimensional flow pattern, breaking spontaneously the initial axisymmetry of the flow. However, all these tiny three-dimensional details emerging at about $t\,(R/g)^{-1/2} = 10^{-4}$ to 10^{-3} are believed to be smoothed out at a timescale of the order of $t\,(R/g)^{-1/2} = 10^{-1}$ to 1, characteristic of the flow development leading to crown formation.

(vii) The entrainment of tiny bubbles described in (ii) and (iv) differs from Mesler entrainment known from literature, and seems to be a new mechanism characteristic of strong impacts on thin liquid films at the wall.

(viii) Summarizing our results in terms of the Weber and Froude numbers, We and Fr, and of the dimensionless film thickness H, we can state, for $0.01 \leqslant H < \infty$, and $2 \leqslant Fr < \infty$, that: at $0 < We \ll 40$ (e.g. already at $We = 2$ and 10) the whole neck region moves outwards; at $40 \ll We < We_c^{(pinch\text{-}off)} \approx 1000$ jetting leading to encapsulation of tiny bubbles occurs; at $We > We_c^{(pinch\text{-}off)} \approx 1000$ jetting leading to pinch-off of the jet tip and formation of tiny droplets occurs.

Note that our results suggest that extrapolation towards very large values of H and Fr is possible. For the characteristic values of the parameters involved (e.g. $W = 10$ and $H \leqslant 0.25$) the Froude number $Fr = WH^{-1/2} \geqslant 20$, and the effect of its variation (as well as that of gravity in general) becomes small. The results show that the dominant effect is related to variation of the Weber number $We = 2\,W^2\,S^{-1}$ (or that of the inverse Bond number S).

(ix) Recognizing that the extremely short times – of the order of $10^{-3}(R/g)^{1/2} \sim 10^{-5}s$ (for $R \sim 1$ mm) – and the small dimensions – of the order of $10^{-2}R \sim 10^{-5}$ m – of the predicted jetting or bubble entrapment, are not readily amenable to experimental investigation, the present numerical study yields some insight into the processes in the neck region under an impinging drop. There are other situations where experimental conditions are so difficult, owing to the short times and small scales involved, that they have not been met to date, and only numerical and analytical results are available, for example, regarding the shape and evolution of the 'air gap' between two colliding drops (Foote 1975; Howison *et al.* 1991). As discussed in § 3.1, the experimental data of Chandra & Avedisian (1991) might be considered to some extent as an indirect confirmation of the tiny-bubble entrapment mechanism in a ring-like region elucidated in the present work. Note that for these data $We = 43$ before impact, effectively increasing after impact owing to heating from the wall.

(x) At weak impacts (e.g. $We \lesssim 10$) jetting does not occur. Accompanied by

capillary waves, the whole neck between the drop and the film at the wall is pulled outwards by surface tension forces instead. This scenario does not lead to bubble entrainment.

(xi) The velocities of the jet tip or the whole neck along the wall may be from 5 up to about 15 times that of the impinging drop; even so, no compressibility effects are involved.

(xii) After a strong impact leading to jetting, at timescales of the order of $t(R/g)^{-1/2} = 10^{-1}$ to 1, a crown is formed in the liquid film at the wall. The crown propagates outwards, at first tilted at its top towards the symmetry axis, subsequently away from it.

(xiii) The main features of the crown found in the present two-dimensional simulations agree with the predictions of the quasi-one-dimensional model of Yarin & Weiss (1995): The crown position varies as $x_c = [C(t - t_0)]^{1/2}$; the crown is preceded by capillary waves; the liquid film at the wall inside the crown is thinner than outside. The crown contains the liquid brought by the drop and scrapes the film as well. There are also signs that a free rim is formed on the top of the crown.

(xiv) The jetting described in (i), and the crown formation of (xii), represent kindred phenomena due to formation of kinematic discontinuity in the velocity distribution in the liquid, leading to outflow from its free surface.

(xv) On a deeper liquid layer, there are signs that the inner wall of the crown may overturn, leading to bubble entrainment in the crater similar to that of Oğuz & Prosperetti (1990).

(xvi) After a weak impact, at $t(R/g)^{-1/2} = 10^{-1}$ to 1, a drop spreads over the wall without crown formation. The leading edge of the spreading spot swells under the action of surface-tension forces.

We are grateful to E.J. Hinch and R.F. Day for very useful discussions. We are indebted for hospitality during our stay at RRC of the University of Wisconsin-Madison. D.A.W. acknowledges with gratitude the financial support by the Swiss National Science Foundation, the Ciba-Geigy-Jubiläumsstiftung, the Israeli Council for Higher Education, and the Swiss Technion Society. A.L.Y. gratefully acknowledges the support of this work under the German-Israeli Foundation Research grant no. I-536-097.14/97, by the Elson/Shapiro Families Research Fund, and by the Fund for the Promotion of the Research at the Technion. Calculations were performed in part on computers provided by the IDRIS and the Technion – IIT.

REFERENCES

Blake, J. R., Taib, B. B. & Doherty, G. 1986 Transient cavities near boundaries. Part 1. Rigid boundary. *J. Fluid Mech.* **170**, 479.

Blake, J. R., Taib, B. B. & Doherty, G. 1987 Transient cavities near boundaries. Part 2. Free surfaces. *J. Fluid Mech.* **181**, 197.

Bowden, F. P. & Field, J. E. 1964 The brittle fracture of solids by liquid impact, by solid impact, and by shock. *Proc. R. Soc. Lond.* A **282**, 331.

Chandra, S. & Avedisian, C. T. 1991 On the collision of a droplet with a solid surface. *Proc. R. Soc. Lond.* A **432**, 13.

Chandrasekhar, S. 1961 *Hydrodynamic and Hydromagnetic Stability*. Clarendon.

Cossali, G. E., Coghe, A. & Marengo, M. 1997 The impact of a single drop on a wetted solid surface. *Exps. Fluids* **22**, 463.

Dooley, B. S., Warncke, A. E., Gharib, M. & Tryggvason, G. 1997 Vortex ring generation due to the coalescence of a water drop at a free surface. *Exps. Fluids* **22**, 369.

Esmailizadeh, L. & Mesler, R. 1986 Bubble entrainment with drops. *J. Colloid Interface Sci.* **110**, 561.

Field, J. E., Dear, J. P. & Ogren, J. E. 1989 The effects of target compliance on liquid drop impact. *J. Appl. Phys.* **65**, 533.

Foote, G. B. 1975 The water drop rebound problem: dynamics of collision. *J. Atmos. Sci.* **32**, 390.

Fukai, J., Shiiba, Y., Yamamoto, T., Miyatake, O., Poulikakos, D., Megaridis, C. M. & Zhao, Z. 1995 Wetting effects on the spreading of a liquid droplet colliding with a flat surface: Experiments and modeling *Phys. Fluids* A **7**, 236.

Fukai, J., Zhao, Z., Poulikakos, D., Megaridis, C. M. & Miyatake, O. 1993 Modeling of the deformation of a liquid droplet impinging upon a flat surface. *Phys. Fluids* A **5**, 2588.

Gao, F. & Sonin, A. A. 1994 Precise deposition of molten microdrops: The physics of digital microfabrication *Proc. R. Soc. Lond.* A **444**, 533.

Hatta, N., Fujimoto, H., Kinoshita, K. & Takuda, H. 1997 Experimental study of deformation mechanism of a water droplet impinging on hot metallic surfaces above the Leidenfrost temperature. *Trans. ASME* I: *J. Fluids Engng* **119**, 692.

Hatta, N., Fujimoto, H. & Takuda, H. 1995 Deformation process of a water droplet impinging on a solid surface. *Trans. ASME* I: *J. Fluids Engng* **117**, 394.

Howison, S. D., Ockendon, J. R. & Wilson, S. K. 1991 Incompressible water-entry problems at small deadrise angles. *J. Fluid Mech.* **222**, 215.

Keller, J. B. & Miksis, M. J. 1983 Surface tension driven flows. *SIAM J. Appl. Maths* **43**, 268.

Lesser, M. B. 1981 Analytic solutions of liquid-drop impact problems. *Proc. R. Sec. Lond.* A **377**, 289.

Lesser, M. B. & Field, J. E. 1983 The impact of compressible liquids. *Ann. Rev. Fluid Mech.* **15**, 97.

Levin, Z. & Hobbs, P. V. 1971 Splashing of water drops on solid and wetted surface: hydrodynamics and charge separation. *Phil. Trans. R. Soc. Lond.* A **269**, 555.

Longuet-Higgins, M. S. & Cokelet, E. D. 1976 The deformation of steep surface waves on water, I. A numerical method of computation. *Proc. R. Soc. Lond.* A **350**, 1.

Lundgren, T. S. & Mansour, N. N. 1988 Oscillations of drops in zero gravity with weak viscous effects. *J. Fluid Mech.* **194**, 479.

Mao, T., Kuhn, D. C. & Tran, H. 1997 Spread and rebound of liquid droplets upon impact on flat surfaces. *AIChE J.* **43**, 2169.

Meier, G. E. A., Klöpper, A. & Grabitz, G. 1992 The influence of kinematic waves on jet break down. *Exps. Fluids* **12**, 173.

Oğuz, H. N. & Prosperetti, A. 1989 Surface-tension effects in the contact of liquid surfaces. *J. Fluid Mech.* **203**, 149.

Oğuz, H. N. & Prosperetti, A. 1990 Bubble entrainment by the impact of drops on liquid surfaces. *J. Fluid Mech.* **219**, 143.

Pasandideh-Fard, M., Qiao, Y. M., Chandra, S. & Mostaghimi, J. 1996 Capillary effects during droplet impact on a solid surface. *Phys. Fluids* **8**, 650.

Peregrine, D. H., Shoker, G. & Symon, A. 1990 The bifurcation of liquid bridges. *J. Fluid Mech.* **212**, 25.

Prosperetti, A. & Oğuz, H. N. 1993 The impact of drops on liquid surfaces and the underwater noise of rain. *Ann. Rev. Fluid Mech.* **25**, 577.

Pumphrey, H. C. & Elmore, P. A. 1990 The entrainment of bubbles by drop impacts. *J. Fluid Mech.* **220**, 539.

Rein, M. 1993 Phenomena of liquid drop impact on solid and liquid surfaces. *Fluid Dyn. Res.* **12**, 61.

Schiaffino, S. & Sonin, A. A 1997*a* Formation and stability of liquid and molten beads on a solid surface. *J. Fluid Mech.* **343**, 95.

Schiaffino, S. & Sonin, A. A. 1997*b* Motion and arrest of a molten contact line on a cold surface: An experimental study. *Phys. Fluids* **9**, 2217.

Shin, J. & McMahon, T. A. 1990 The tuning of a splash. *Phys. Fluids* A **2**, 1312.

Stow, C. D. & Hadfield, M. G. 1981 An experimental investigation of fluid flow resulting from the impact of a water drop with an unyielding dry surface. *Proc. R. Soc. Lond.* A **373**, 419.

Waldvogel, J. M. & Poulikakos, D. 1997 Solidification phenomena in picoliter size solder droplet deposition on a composite substrate. *Intl J. Heat Mass Transfer* **40**, 295.

Weiss, D. A. 1997 Quelques études d'écoulements incompressibles. Dossier en vue de l'habilitation à diriger des recherches. Université Pierre et Marie Curie, Paris (in French).

Worthington, A. M. 1876 On the forms assumed by drops of liquids falling vertically on a horizontal plate. *Proc. R. Soc. Lond.* A **25**, 261.

Worthington, A. M. 1877 A second paper on the forms assumed by drops of liquids falling vertically on a horizontal plate. *Proc. R. Soc. Lond.* A **25**, 498.

Worthington, A. M. 1908 *A Study of Splashes.* Longmans, Green.

Yarin, A. L. & Weiss, D. A. 1995 Impact of drops on solid surfaces: self-similar capillary waves, and splashing as a new type of kinematic discontinuity. *J. Fluid Mech.* **283**, 141.

Zimon, A. D. 1982 *Adhesion of Dust and Powder.* Plenum.